How to cite: *Angew. Chem. Int. Ed.* **2023**, *62*, e202300302
doi.org/10.1002/anie.202300302

2D Materials

Phase Instability in van der Waals In_2Se_3 Determined by Surface Coordination

*Shanru Yan[+], Chao Xu[+], Cenchen Zhong, Yancong Chen, Xiangli Che, Xin Luo, and Ye Zhu**

Abstract: van der Waals In_2Se_3 has attracted significant attention for its room-temperature 2D ferroelectricity/antiferroelectricity down to monolayer thickness. However, instability and potential degradation pathway in 2D In_2Se_3 have not yet been adequately addressed. Using a combination of experimental and theoretical approaches, we here unravel the phase instability in both α- and β′-In_2Se_3 originating from the relatively unstable octahedral coordination. Together with the broken bonds at the edge steps, it leads to moisture-facilitated oxidation of In_2Se_3 in air to form amorphous $In_2Se_{3-3x}O_{3x}$ layers and Se hemisphere particles. Both O_2 and H_2O are required for such surface oxidation, which can be further promoted by light illumination. In addition, the self-passivation effect from the $In_2Se_{3-3x}O_{3x}$ layer can effectively limit such oxidation to only a few nanometer thickness. The achieved insight paves way for better understanding and optimizing 2D In_2Se_3 performance for device applications.

Introduction

As a chalcogenide semiconductor in the III_2-VI_3 family, In_2Se_3 has a complex phase diagram consisting of a variety of polymorphs with distinct bonding geometry, just like many other metal chalcogenides.[1–4] The two room-temperature phases, α- and β′-In_2Se_3, and the high-temperature β phase have the 2D layered structure consisting of [Se–In–Se–In–Se] quintuple layers bonded by the vdW force, with several stacking orders (2H, 3R, 1T) available for each phase.[5–8] Within each quintuple layer, β′- and β-In_2Se_3 have all the In atoms octahedrally coordinated by Se atoms, whereas α-In_2Se_3 have only one layer of In atoms octahedrally coordinated and the other In layer with tetrahedral coordination.[8–10] More excitingly, the asymmetric bonding of the central-layer Se atoms breaks centrosymmetry and leads to spontaneous electric polarization along both in-plane and out-of-plane directions.[10] It makes α-In_2Se_3 an emerging 2D semiconductor with room-temperature ferroelectricity down to single-layer thickness.[11–13] Similar ferroelectric structure distortion originating from the central-layer Se atoms has also been identified recently in β′-In_2Se_3, which however is spatially modulated to form the characteristic superstructure consisting of periodic nanostripes. Such nanostriped superstructure demonstrates unusual 2D antiferroelectricity, which distinguishes it from the high-temperature paraelectric β phase.[14] The unique structure of In_2Se_3 gives rise to extraordinary properties such as broad-range light absorption,[15] high photosensitivity and quick photoresponse,[16] ultrathin ferroelectricity/antiferroelectricity,[10–14] 2D ferroelasticity,[17] and giant pyroelectricity.[18] Significant research efforts have been devoted to exploring their application potential as optoelectronics,[19–21] ferroelectric field-effect transistors (FETs),[22] nonvolatile memories,[11,23] and piezoelectric nanogenerators.[24]

As predicted by the In–Se–O phase diagram, indium selenide can be oxidized to form In_2O_3 and $In_2(SeO_4)_3$,[25,26] making its stability a particular issue for device applications.[27] Early studies have shown that oxidation on InSe single crystals does not occur in air at room temperature, unless sputtering is applied to create vacancies and broken bonds, or temperature is raised to initiate thermal oxidation.[25,26,28] However, the recent study on ultrathin InSe flakes demonstrates room-temperature oxidation in both pure O_2 and air, with the latter being more substantial due to the presence of moisture.[27] Such oxidation causes p-type doping in the InSe semiconductor and leads to current hysteresis in 2D device operation. The susceptibility of ultrathin InSe flakes to oxidation can be attributed to the band gap change at different thicknesses,[27] while the presence of defects such as Se vacancies in the ultrathin flakes may also promote the oxidation process.[29,30] As for In_2Se_3, oxidation of microplates has also been reported to form the $In_2Se_{3-3x}O_{3x}$ surface layer.[29] On the other hand, for

[*] S. Yan,[+] Dr. C. Xu,[+] C. Zhong, Dr. X. Che, Dr. Y. Zhu
Department of Applied Physics, Research Institute for Smart Energy, The Hong Kong Polytechnic University
Hung Hom, Kowloon, Hong Kong (P.R. China)
E-mail: yezhu@polyu.edu.hk

Y. Chen, Prof. X. Luo
State Key Laboratory of Optoelectronic Materials and Technologies, Guangdong Provincial Key Laboratory of Magnetoelectric Physics and Devices, Centre for Physical Mechanics and Biophysics, School of Physics, Sun Yat-sen University
Guangzhou (P.R. China)

[+] These authors contributed equally to this work.

2D In_2Se_3 flakes that are relevant to ultrathin device applications, their stability issue has not yet been adequately addressed. In particular, the lack of centrosymmetry in In_2Se_3 leads to distinct surfaces with different ferroelectric polarization and bonding geometry. Whether the stability of In_2Se_3 may depend on the type of exposed surface is currently unknown, leaving a knowledge gap that hampers both device mechanistic understanding and performance optimization.

Here we present a systematic study on phase stability in both α-In_2Se_3 and β′-In_2Se_3 2D flakes at room temperature. Using a combination of optical and electron microscopy/spectroscopy, we detect the reaction of In_2Se_3 with air to form the amorphous $In_2Se_{3-3x}O_{3x}$ surface layer with Se hemisphere particles precipitating on top. Atomic-force microscopy (AFM) further allows us to identify the nucleation sites of Se particles and to measure their size and volume quantitatively to derive the growth behavior. Applying these characterization techniques on various In_2Se_3 surfaces, we successfully elucidate the decisive role of surface coordination, with the octahedral coordination being less stable and leading to more Se particle formation compared to tetrahedral coordination, which has also been consolidated by first-principles calculations. The In_2Se_3 phase instability in the controlled environment has also been investigated to pinpoint the reaction mechanism as well as the effect of light illumination.

Results and Discussion

The instability of α-In_2Se_3 in air is illustrated in Figure 1. After one week air exposure, the optical image reveals the formation of many particles a few hundred nm in size on the surface (Figure 1b), which do not exist on the as-exfoliated flake (Figure 1a). Energy-dispersive X-ray spectroscopy (EDS) in scanning electron microscopy (SEM) detects much higher Se content in the particles (In:Se = 2:19.8) than on the clean surface (In:Se = 2:3.1), as shown in Figure 1c, suggesting that the reaction products are Se particles escaping from In_2Se_3 lattice. This is further confirmed by Raman spectroscopy shown in Figure 1d: compared to the clean surface that displays five characteristic peaks of α-In_2Se_3,[31] the surface particle exhibits an additional peak at ≈250 cm^{-1} (region II in Figure 1d), which corresponds to pure Se.[32] Ultrathin α-In_2Se_3 flakes exhibit the same surface reaction in air, as demonstrated in Supporting Figure S1.

To probe the reacted phase on the finer scale, we have used focused-ion beam (FIB) to prepare cross-sectional transmission electron microscopy (TEM) samples across the surface particles and carried out aberration-corrected scan-

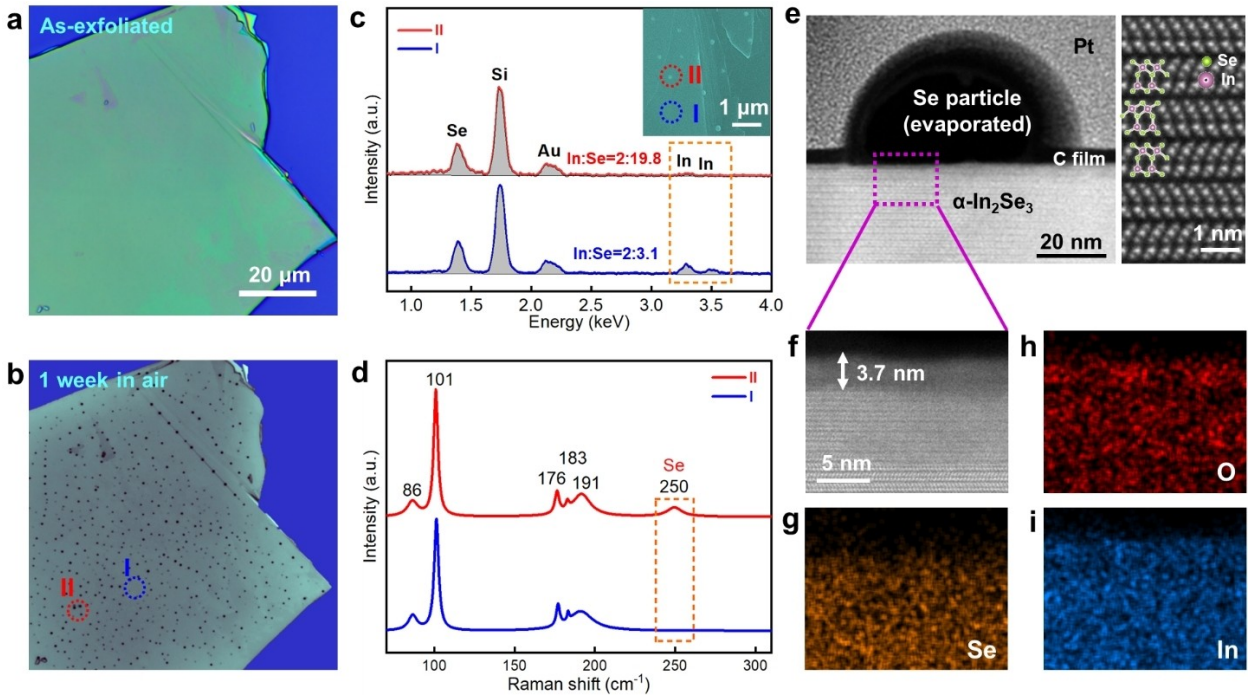

Figure 1. a), b) Optical micrographs of the same α-In_2Se_3 flake (a) right after exfoliation and (b) after one week air exposure, showing the development of surface particles. c) SEM-EDS taken from the regions indicated in the inset SEM image, showing much higher Se content in the surface particle (red) than in the flat region (blue). d) Raman spectroscopy acquired from the regions circled in (b), showing the pure Se signal (≈250 cm^{-1}) from the surface particle that is not present from the flat surface. The characteristic peaks at 86 cm^{-1}, 101 cm^{-1}, and 176–191 cm^{-1} correspond to the E, A_1(LO + TO), and A_1(TO) vibration modes of α-In_2Se_3,[31] respectively. e) Annular dark-field (ADF) STEM image showing the hemisphere cavity left by Se evaporation on the top surface, with the atomic-resolution STEM image on the right illustrating its atomic structure. f) Magnified ADF-STEM image from the region indicated in (e) and h–i) simultaneous EDS maps for (h) O, (g) Se, and (i) In, respectively, showing the amorphous $In_2Se_{3-3x}O_{3x}$ surface layer. The α-In_2Se_3 flake is ≈480 nm thick on a SiO_2/Si substrate (See Supporting Figure S2).

ning TEM (STEM) observation. Even though Se evaporated[28] during the ion-milling process in vacuum, it still left a hemisphere cavity capped by C and Pt protection layers (Figure 1e), reflecting the original shape of the surface Se particle as also verified by AFM (Supporting Figure S3). Atomic-resolution STEM image further identifies an amorphous layer ≈3.7 nm on the top surface (Figure 1f) which is O rich and Se deficient as unveiled by STEM-EDS mapping (Figures 1g and h). The O-rich amorphous layers are present underneath every Se particles, with another example shown in Supporting Figure S4. For comparison, the as-exfoliated flake shows a clean surface without such an oxygen-rich amorphous layer (Supporting Figure S5). Altogether, Figure 1 indicates that air can react with α-In_2Se_3 through substituting surface Se with O, which gives rise to an amorphous $In_2Se_{3-3x}O_{3x}$ surface layer, while the replaced Se precipitates to form hemisphere particles on the surface. The observed less In in the top surface layer (Figure 1i) may be attributed to the less dense structure of amorphous $In_2Se_{3-3x}O_{3x}$ compared to the α-In_2Se_3 lattice. We note that even though the air-induced $In_2Se_{3-3x}O_{3x}$ layer on the In_2Se_3 surface at room temperature has been identified by X-ray photoelectron spectroscopy (XPS),[29] its amorphous nature and the accompanied Se particle formation has never been reported previously.

More interestingly, the two complementary surfaces of α-In_2Se_3 created by exfoliation (see Figure 2a and EXPERIMENTAL SECTION) show dissimilar instability. As evinced in Figure 2, after one week air exposure under exactly the same condition, one of the complementary surfaces (plane A) develops more Se particles (Figure 2d) than the other (plane B in Figure 2e). Based on the surface topography probed by AFM (Figures 2f and g), we also derive the total volume of Se particles per unit surface area as $\approx 8.4\times10^5\ nm^3\,\mu m^{-2}$ for plane A and $\approx 1.1\times10^5\ nm^3\,\mu m^{-2}$ for plane B. The high resolution and surface sensitivity of AFM enable us to further identify the nucleation sites of Se particles: As one of the unique properties of 2D materials, the basal-plane-terminated surfaces are free of broken bonds and thus relatively stable. Only at the step edges there are exposed atoms with reduced coordination and broken bonds, making them the active sites for both electrochemical reactions[33–36] and degradation.[37–39] Indeed, AFM reveals that surface Se particles nearly all form along the step edges of plane B (Figure 2g), consistent with above consideration. On the other hand, despite the same amount of step edges on the two complementary surfaces, Se particles on plane A grow uniformly not only along the step edges but also on the flat surface (Figure 2f), accounting for their larger population compared with those on plane B (also see Supporting Figure S6).

The dissimilar nucleation behaviour and the associated surface particle population demonstrate distinct phase stability between the two complementary surfaces. This is not surprising given the anisotropic structure of α-In_2Se_3, especially along the out-of-plane direction, which leads to opposite polarization as well as different surface coordination for the two complementary surfaces (Figure 2a). Using both piezoresponse force microscopy (PFM) and Kelvin probe force microscopy (KPFM, see Supporting Note 1 and Figure S7), we have explicitly determined the directions of out-of-plane polarization as downward (upward) for plane A (B). It also means that plane A has the octahedral coordination on the surface, in contrast to the tetrahedral coordination for plane B, as confirmed by atomic-resolution STEM imaging (Figure 2a). Nevertheless, to pinpoint ex-

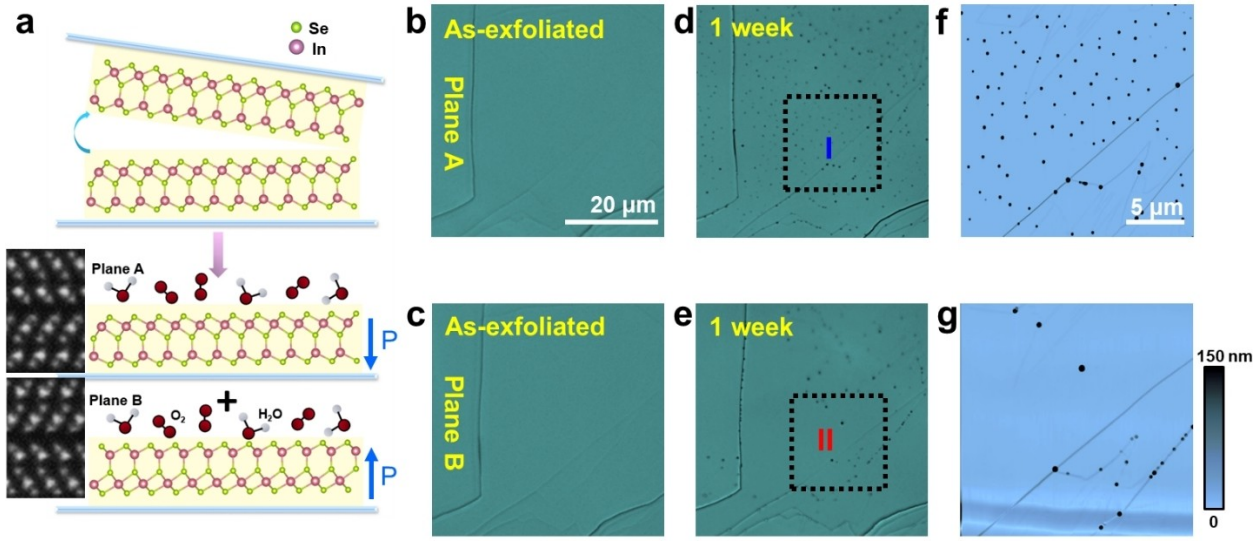

Figure 2. Surface-dependent instability in α-In_2Se_3. a) Schematic of the exfoliation process to create two fresh complementary surfaces with opposite polarization and distinct surface coordination, with the atomic-resolution STEM images on the left. b)–e) Optical micrographs of the complementary surfaces with the same amount of step edges (b, c) right after exfoliation and (d, e) after one week air exposure, and f), g) AFM topography maps acquired from the squared regions in (d, e) for (b, d, f) plane A and (c, e, g) B, respectively. After air exposure under exactly the same condition, plane A shows much more surface particles than plane B (105 vs. 21 particles per 400 μm^2), indicating more Se escaping from α-In_2Se_3 lattice.

actly what determines the stability of α-In_2Se_3, we need to first decouple the two factors of electric polarization and surface coordination.

Different from α-In_2Se_3 that is ferroelectric, β′-In_2Se_3 possesses in-plane antiferroelectricity at room temperature,[14] with octahedral-coordinated In only (Figure 3i) and no out-of-plane polarization. It thus provides an ideal system to examine the stability of octahedral surface coordination without complication from electric polarization. As shown in Figure 3, β′-In_2Se_3 exhibits the similar instability during air exposure, with the formation of surface Se particles (Figures 3a and b) on top of an amorphous $In_2Se_{3-3x}O_{3x}$ surface layer (Supporting Figure S4). However, in contrast to α-In_2Se_3 whose complementary surfaces show dissimilar instability, the two complementary surfaces of β′-In_2Se_3 after air exposure show nearly the same population of Se particles ($\approx 8.4\times10^5$ vs. 8.2×10^5 $nm^3\,\mu m^{-2}$ from Figures 3g and h) that is remarkably close to plane A of α-In_2Se_3 ($\approx 8.4\times10^5$ $nm^3\,\mu m^{-2}$). AFM also reveals that on both surfaces, the Se particles develop uniformly not only along the step edges but also at the flat regions (Figures 3g and h), the same nucleation behavior as plane A of α-In_2Se_3 (Figure 2f). One characteristic of β′-In_2Se_3 is the presence of ferroelastic domain walls,[17] which does not exist in α-In_2Se_3. Polarized light microscopy on reacted β′-In_2Se_3 surface further shows no apparent correlation between the precipitated Se particles and domain walls (Supporting Figure S8). Given that both surfaces of β′-In_2Se_3 have octahedral coordination, just like plane A of α-In_2Se_3, this clearly indicates that the phase stability of In_2Se_3 mainly depends on the surface coordination rather than polarization, with octahedral coordination being less stable compared to tetrahedral coordination.

The discovered instability of octahedral-coordinated In_2Se_3 relative to tetrahedral coordination is consistent with Ref [9], which attributes it to the unstable antibonding states of the octahedral-coordinated In atoms. Indeed, our first-principles Crystal Orbital Hamilton Population (COHP) calculation (see EXPERIMENTAL SECTION) unveils small amount of antibonding states below the Fermi level for the octahedral-coordinated In atoms in both α-In_2Se_3 (black curve in Supporting Figure S9c) and β′-In_2Se_3 (Supporting Figure S9d), which should destabilize the In–Se octahedra and contribute to the above identified phase instability. While for the tetrahedral-coordinated In atoms, such antibonding states are negligible (red curve in Supporting Figure S9c), which explains the better stability of plane B compared to plane A observed in α-In_2Se_3 (Figure 2).

Besides comparing the antibonding states, we also evaluate the phase stability by estimating the energy cost associated with charge transfer. Given that In is positively charged and Se is negatively charged in In_2Se_3 (see Supporting Figures S9a and S9b), forming pure Se particles requires Se anions in In_2Se_3 to lose electrons. We thus consider the electron transfer from lattice Se in the top-most layer to neighbouring In as an intermediate process for degradation, and determine its energy cost using density

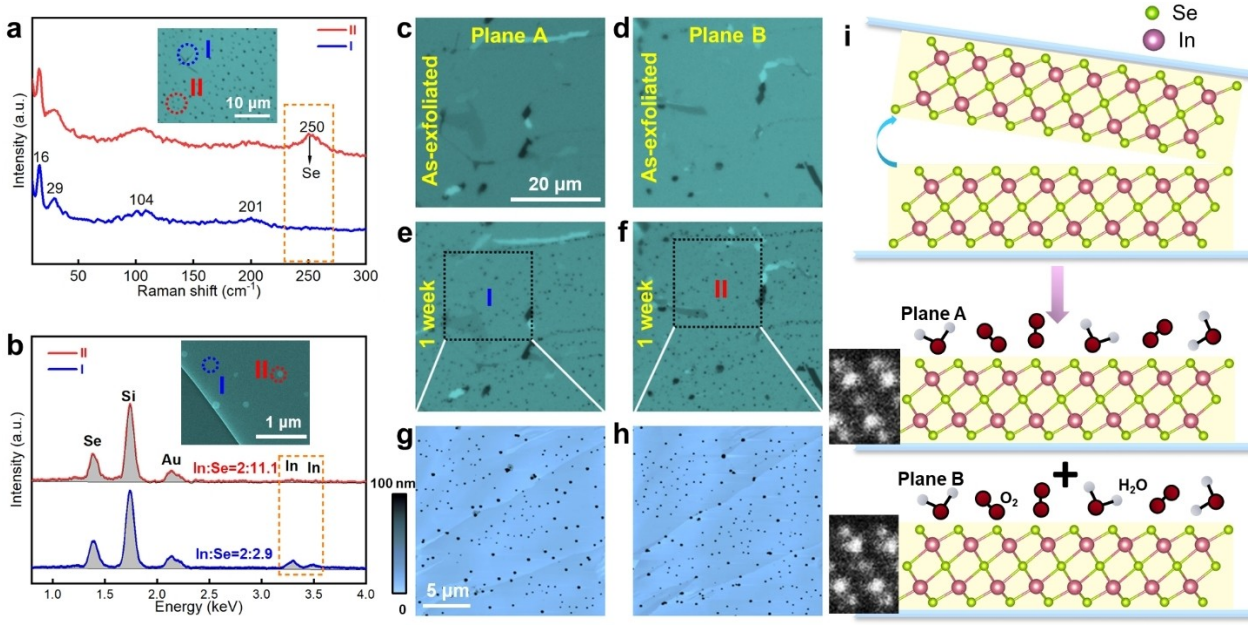

Figure 3. Similar instability on the two complementary surfaces of β′-In_2Se_3. a) Raman spectroscopy acquired from the regions circled in the inset optical micrograph, showing the pure Se signal ($\approx$250 cm^{-1}) from the surface particle that is not present from the flat surface. The four characteristic peaks at 16 cm^{-1}, 29 cm^{-1}, 104 cm^{-1}, and 201 cm^{-1} reflect four typical vibration modes of β′-In_2Se_3.[17] b) SEM-EDS taken from the regions indicated in the inset SEM image, showing much higher Se content in the surface particle (red) than in the flat region (blue). c)–f) Optical micrographs of the complementary surfaces (c,d) right after exfoliation and (e, f) after one week air exposure, and g), h) AFM topography maps acquired from the squared regions in (e, f) for (c, e, g) plane A and (d, f, h) B, respectively. Both surfaces show indistinguishable behavior, which is also very similar to plane A in α-In_2Se_3. i) Schematic of the exfoliation process to create two fresh complementary surfaces with the same octahedral coordination, with the atomic-resolution STEM images on the left.

functional theory (DFT) calculation. As depicted in Figure S10, electron transfer from surface Se to the octahedral-coordinated In demands ≈3.2 eV/e$^-$ energy for α-In_2Se_3 (Supporting Figure S10b) and ≈3.1 eV/e$^-$ energy for β′-In_2Se_3 (Supporting Figures S10c and S10d), much lower than ≈4.2 eV/e$^-$ energy for tetrahedral-coordinated In (Supporting Figure S10a). It further indicates that degradation is more energetically favourable for the octahedral-coordinated surface, in consistency with our experimental observation. We note that the above calculations only account for phase instability on the basal-plane-terminated surfaces without broken bonds. Surface edge steps with dangling bonds should be more active and unstable, and serve as the nucleation sites of Se particles for all the characterized surface planes including plane B of α-In_2Se_3 with the stable tetrahedral coordination (Figures 2e and g). Such particles are nearly uniformly distributed around the whole edge of α-In_2Se_3 flakes without preferential nucleation along any direction (Supporting Figure S11), which excludes the potential effect of in-plane polarization and indicates that surface dangling bonds should play the dominant role in the Se particle formation at edge steps.

With the elucidated instability as the driving force for In_2Se_3 degradation, we next study the detailed degradation behavior by monitoring the volume of surface Se particles in air using AFM. As shown in Figure 4, within one hour after exfoliation, Se particles quickly develop at both edge steps and flat surfaces of β′-In_2Se_3 flakes (Figure 4a). The average particle volume grows faster during the first 12 hour air exposure, and then increases linearly for about one week, after which the growth is nearly saturated. Such a behavior suggests that degradation of In_2Se_3 is confined near the surface, with the degradation rate declining as the surface In_2Se_3 is consumed. Degradation stops when the surface is completely converted into amorphous $In_2Se_{3-3x}O_{3x}$, reflecting a self-passivation effect that can protect the inner material from further degradation. Indeed, cross-sectional STEM imaging has revealed that degradation of In_2Se_3 is limited to a <4 nm surface layer when the saturation occurs after one week air exposure (Figure 1f and Supporting Figure S4). It has been reported that oxidation on ultrathin InSe flakes can give rise to a surface passivation layer that can retard further oxidation.[27] Our observation in Figure 4 demonstrates the same self-passivation effect on In_2Se_3 flakes, suggesting that degradation in In_2Se_3 may not be a problem when utilizing its bulk properties. On the other hand, for devices based on the surface/interface of In_2Se_3 or ultrathin In_2Se_3, the quick formation of amorphous $In_2Se_{3-3x}O_{3x}$ surface layer may need to be avoided by either limiting the air exposure within a few minutes or using the tetrahedral-coordinated surface with minimal step edges.

In spite of the above general behavior, the particles at edge steps are consistently larger than those on flat surfaces, indicating that the surface dangling bonds at edge steps favors the Se particle formation more than the octahedral coordination. We have explicitly compared the Se particle growth at edge steps on the two complementary surfaces of α-In_2Se_3 (with the same density of edge steps) as shown in Supporting Figure S12: Both plane A and B exhibit the similar growth behavior, suggesting that Se particle precipitation at edge steps is independent of either surface coordination or polarization effects. During the particle growth, the particle density actually decreases (blue curve in Figure 4b) owing to the disappearance of small particles by either Oswald ripening or coalescence as observed in Figures 4e and f explicitly. It suggests that Se atoms are highly mobile and can easily diffuse around on the In_2Se_3 surface to facilitate the particle growth, which has also been directly observed in Supporting Figure S13. Presumably for this reason, new Se particles cannot nucleate without being quickly consumed by the big particles nearby. Nevertheless, the total volume of surface Se particles still rises (blue curve in Figure 4d) with the similar trend as the average particle volume (Figure 4c), demonstrating more Se escaping from In_2Se_3 lattice upon continuous air exposure until saturation occurs.

The above degradation behavior is observed under white light illumination. Given the broad-range light absorption and high photosensitivity of In_2Se_3, it is interesting to assess the role of light illumination on the In_2Se_3 degradation behavior. As demonstrated in Figures 4c and d, blocking light does not alter the general rising trend of both the average and total Se particle volumes (red curves), but only makes it slower. As measured from the linear growth regime in Figure 4d, light illumination can enhance the growth rate of Se particles by over 1.5 fold, likely by generating more charge carriers and promoting the charge transfer process to form surface Se particles. Interestingly, the comparison in Figure 4b reveals the significantly decreased particle density upon light illumination, as also illustrated in Supporting Figure S14, reflecting the enhanced Se mobility to facilitate the Oswald ripening and coalescence processes, which further leads to a much higher particle growth rate shown in Figure 4c.

At last, we try to pinpoint the reaction mechanism for In_2Se_3 surface degradation. The formation of amorphous $In_2Se_{3-3x}O_{3x}$ surface layer immediately suggests the following oxidation reaction:

$$In_2Se_3 + \frac{3x}{2}O_2 \rightarrow In_2Se_{3-3x}O_{3x} + 3xSe \quad (1)$$

which is indeed favored by thermodynamics.[25] However, after exposing to pure O_2 for 10 days, no Se particles can be observed in both α-In_2Se_3 and β′-In_2Se_3 (Supporting Figures S15c and S15d). Further exposure to air for 2 days leads to obvious particle formation on both samples (Supporting Figures S15e and S15f), indicating that O_2 itself is not sufficient to oxidize In_2Se_3 at room temperature, and H_2O moisture may be essential for the formation of surface $In_2Se_{3-3x}O_{3x}$ layer and Se particles. A similar trend is observed for the growth of Se particles as summarized in Figure 5a: After the initial formation of Se particles upon air exposure, subsequent 2-day exposure to pure O_2 leads to negligible particle growth for all 6 tracked particles, indicating little Se escaping caused by O_2. It demonstrates that oxidation of In_2Se_3 in pure O_2 is very slow at room temperature, consistent with the early studies on InSe single

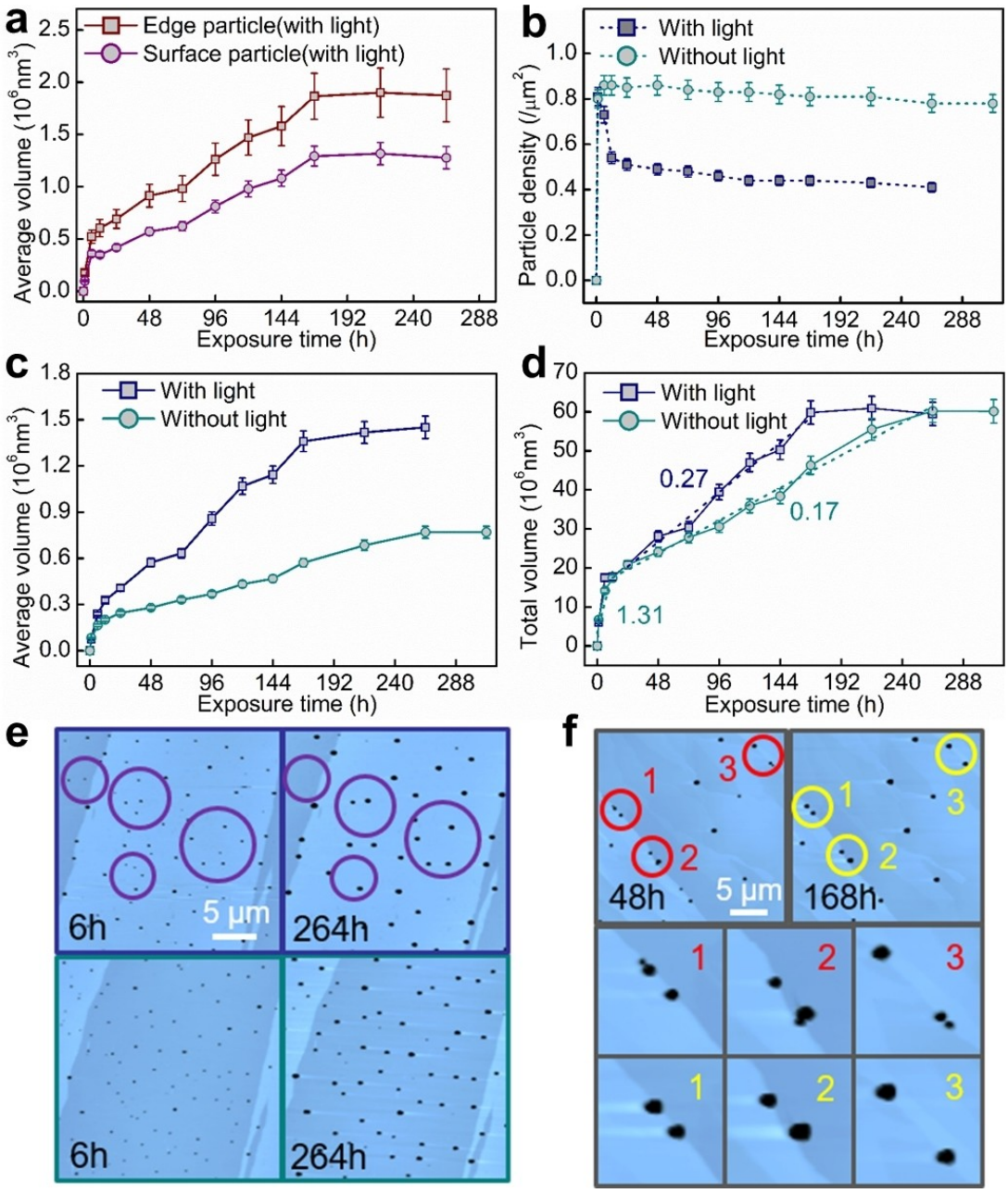

Figure 4. Behavior of Se particle growth on the surface of β′-In_2Se_3. a) Average volumes of Se particles at the edge steps and on the flat surface under light illumination measured by AFM as functions of time. b) Area densities of surface Se particles as functions of time with and without light illumination. c) Average and d) total volumes of surface Se particles as functions of time with and without light illumination. The slopes for the linear-growth regime in (d) are indicated, showing the acceleration of Se particle growth by light illumination. e), f) AFM topography maps on the complementary surfaces of β′-In_2Se_3, showing decreased particle density in the circled regions due to (e) Oswald ripening and (f) coalescence under light illumination.

crystals that can only be oxidized upon sputtering or at elevated temperature.[25,26,28] Switching back to air exposure resumes apparent particle growth, confirming the essential role of moisture in both nucleation and growth of Se particles.

On the other hand, submerging In_2Se_3 flakes in degassed liquid H_2O (to remove O_2, see EXPERIMENTAL SECTION) as well as H_2O moisture for one week does not generate any Se particles either (Figure 5). Cross-sectional STEM imaging further evinces the amorphous surface layer to be thinner than one quintuple layer (Figure 5b), representing very slow degradation if any. Therefore, both O_2 and H_2O moisture are required to degrade In_2Se_3, just as the degradation of black phosphorous in ambient conditions,[41] with H_2O possibly serving as a catalyst to overcome the sluggish kinetics of In_2Se_3 oxidation, similar to the oxidation of few-layer black phosphorous catalyzed by water in a dark environment.[42] This is also in line with the previous report

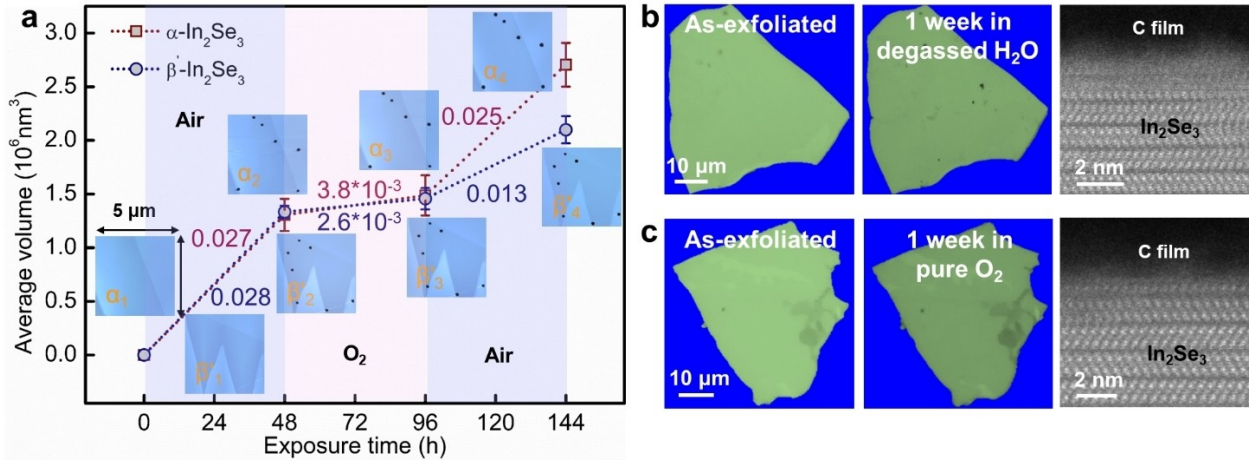

Figure 5. a) Average volume of surface Se particles measured by AFM on both α- and β′-In_2Se_3 as a function of time exposure to the controlled atmosphere, showing negligible particle growth in pure oxygen. b), c) Optical micrographs and the associated cross-sectional STEM images of β′-In_2Se_3 flakes before and after one week exposure to (b) degassed water and (c) pure oxygen, showing no formation of surface particles and amorphous surface layers. The flake thicknesses are 440 nm for (b) and 55 nm for (c), respectively, both on the SiO_2/Si substrates.

showing faster oxidation of InSe in humid air than in dry air.[27,40] Theoretical study has also shown that InSe can spontaneously adsorb and decompose water molecules on the surface and lose electrons during this process,[40] which presents a feasible mechanism for oxidation and Se particle formation on In_2Se_3.[30] While the detailed role of H_2O moisture in In_2Se_3 oxidation still needs further investigation.

Conclusion

In summary, using a combination of experimental and theoretical approaches, we have unraveled the phase instability in α- and β′-In_2Se_3 originating from the relatively unstable octahedral coordination. Together with the broken bonds at the edge steps, it leads to the reaction of In_2Se_3 with air to form amorphous $In_2Se_{3-3x}O_{3x}$ surface layers, with Se hemisphere particles precipitating on top. Both oxygen and moisture are required for such surface oxidation, which can be further promoted by light illumination. Therefore, for devices based on ultrathin In_2Se_3 or the clean surface of In_2Se_3, it may be necessary to minimize the air exposure during fabrication, or using the tetrahedral-coordinated surface with minimal step edges. On the other hand, the formed $In_2Se_{3-3x}O_{3x}$ layer can self-passivate the surface and limit oxidation to only a few nanometer thickness, indicating that degradation in In_2Se_3 may not be a problem when utilizing its bulk properties. The achieved insight on the In_2Se_3 instability paves way for better understanding and optimizing its performance for device applications.

Acknowledgements

Y.Z. is thankful for the financial support from the Research Grants Council of Hong Kong (General Research Fund No. 15305718) and the Hong Kong Polytechnic University (Grant No. ZVRP). X.L. acknowledge the support from National Natural Science Foundation of China (Grants No. 12172386), the National Natural Science Foundation of Guangdong Province, China (Grant No. 2021B1515020021), and the Fundamental Research Funds for the Central Universities, Sun Yat-sen University. The TEM facility is funded by the Research Grants Council of Hong Kong (Project No. C5029-18E).

Conflict of Interest

The authors declare no conflicts of interest.

Data Availability Statement

The data that support the findings of this study are available in the Supporting Information of this article.

Keywords: Chalcogenides · Ferroelectric Materials · 2D Materials · Phase Stability · Surface Oxidation

[1] C. Peng, L. C. Wu, Z. T. Song, F. Rao, M. Zhu, X. L. Li, B. Liu, L. M. Cheng, S. L. Feng, P. X. Yang, J. H. Chu, *Appl. Surf. Sci.* **2011**, *257*, 10667–10670.
[2] S. M. Souza, C. M. Poffo, D. M. Trichês, J. C. de Lima, T. A. Grandi, A. Polian, M. Gauthier, *Phys. B* **2012**, *407*, 3781–3789.
[3] J. G. Zhao, H. Z. Liu, L. Ehm, D. W. Dong, Z. Q. Chen, G. D. Gu, *J. Phys. Condens. Matter* **2013**, *25*, 125602.
[4] Z. H. Yu, L. Wang, Q. Y. Hu, J. G. Zhao, S. Yan, K. Yang, S. Sinogeikin, G. D. Gu, H. K. Mao, *Sci. Rep.* **2015**, *5*, 15939.
[5] J. Van Landuyt, G. Van Tendeloo, S. Amelinckx, *Phys. Status Solidi A* **1975**, *30*, 299–314.
[6] C. Manolikas, *J. Solid State Chem.* **1988**, *74*, 319–328.
[7] X. Tao, Y. Gu, *Nano Lett.* **2013**, *13*, 3501–3505.

[8] L. X. Liu, J. Y. Dong, J. Q. Huang, A. M. Nie, K. Zhai, J. Y. Xiang, B. C. Wang, F. S. Wen, C. P. Mu, Z. S. Zhao, Y. J. Gong, Y. J. Tian, Z. Y. Liu, *Chem. Mater.* **2019**, *31*, 10143–10149.
[9] M. Küpers, P. M. Konze, A. Meledin, J. Mayer, U. Englert, M. Wuttig, R. Dronskowski, *Inorg. Chem.* **2018**, *57*, 11775–11781.
[10] W. J. Ding, J. B. Zhu, Z. Wang, Y. F. Gao, D. Xiao, Y. Gu, Z. Y. Zhang, W. G. Zhu, *Nat. Commun.* **2017**, *8*, 14956.
[11] C. J. Cui, W. J. Hu, X. X. Yan, C. Addiego, W. P. Gao, Y. Wang, Z. Wang, L. Z. Li, Y. C. Cheng, P. Li, X. X. Zhang, H. N. Alshareef, T. Wu, W. G. Zhu, X. Q. Pan, L. J. Li, *Nano Lett.* **2018**, *18*, 1253–1258.
[12] F. Xue, W. J. Hu, K. C. Lee, L. S. Lu, J. W. Zhang, H. L. Tang, A. Han, W. T. Hsu, S. B. Tu, W. H. Chang, C. H. Lien, J. H. He, Z. D. Zhang, L. J. Li, X. X. Zhang, *Adv. Funct. Mater.* **2018**, *28*, 1803738.
[13] J. Xiao, H. Y. Zhu, Y. Wang, W. Feng, Y. X. Hu, A. Dasgupta, Y. M. Han, Y. Wang, D. A. Muller, L. W. Martin, P. A. Hu, X. Zhang, *Phys. Rev. Lett.* **2018**, *120*, 227601.
[14] C. Xu, Y. C. Chen, X. B. Cai, A. Meingast, X. Y. Guo, F. K. Wang, Z. Y. Lin, T. W. Lo, C. Maunders, S. Lazar, N. Wang, D. Y. Lei, Y. Chai, T. Y. Zhai, X. Luo, Y. Zhu, *Phys. Rev. Lett.* **2020**, *125*, 047601.
[15] B. Tang, L. F. Hou, M. Sun, F. J. Lv, J. H. Liao, W. Ji, Q. Chen, *Nanoscale* **2019**, *11*, 12817–12828.
[16] T. Y. Zhai, X. S. Fang, M. Y. Liao, X. J. Xu, L. Li, B. D. Liu, Y. Koide, Y. Ma, J. N. Yao, Y. Bando, D. Golberg, *ACS Nano* **2010**, *4*, 1596–1602.
[17] C. Xu, J. F. Mao, X. Y. Guo, S. R. Yan, Y. C. Chen, T. W. Lo, C. S. Chen, D. Y. Lei, X. Luo, J. H. Hao, C. X. Zheng, Y. Zhu, *Nat. Commun.* **2021**, *12*, 3665.
[18] J. Jiang, L. F. Zhang, C. Ming, H. Zhou, P. Bose, Y. W. Guo, Y. Hu, B. W. Wang, Z. Z. Chen, R. Jia, S. Pendse, Y. Xiang, Y. B. Xia, Z. H. Lu, X. X. Wen, Y. Cai, C. L. Sun, G. C. Wang, T. M. Lu, D. Gall, Y. Y. Sun, N. Koratkar, E. Fohtung, Y. F. Shi, J. Shi, *Nature* **2022**, *607*, 480–485.
[19] M. Lin, D. Wu, Y. Zhou, W. Huang, W. Jiang, W. S. Zheng, S. L. Zhao, C. H. Jin, Y. F. Guo, H. L. Peng, Z. F. Liu, *J. Am. Chem. Soc.* **2013**, *135*, 13274–13277.
[20] J. D. Zhou, Q. S. Zeng, D. H. Lv, L. F. Sun, L. Niu, W. Fu, F. C. Liu, Z. X. Shen, C. H. Jin, Z. Liu, *Nano Lett.* **2015**, *15*, 6400–6405.
[21] H. H. Shi, M. M. Li, A. Shaygan Nia, M. C. Wang, S. W. Park, Z. Zhang, M. R. Lohe, S. Yang, X. L. Feng, *Adv. Mater.* **2020**, *32*, 1907244.
[22] M. W. Si, A. K. Saha, S. J. Gao, G. Qiu, J. K. Qin, Y. Q. Duan, J. Jian, C. Niu, H. Y. Wang, W. Z. Wu, S. K. Gupta, P. D. Ye, *Nat. Electron.* **2019**, *2*, 580–586.
[23] M. S. Choi, B. K. Cheong, C. H. Ra, S. Y. Lee, J. H. Bae, S. W. Lee, G. D. Lee, C. W. Yang, J. Hone, W. J. Yoo, *Adv. Mater.* **2017**, *29*, 1703568.
[24] F. Xue, J. W. Zhang, W. J. Hu, W. T. Hsu, A. L. Han, S. F. Leung, J. K. Huang, Y. Wan, S. H. Liu, J. L. Zhang, J. H. He, W. H. Chang, Z. L. Wang, X. X. Zhang, L. J. Li, *ACS Nano* **2018**, *12*, 4976–4983.
[25] O. A. Balitskii, N. N. Berchenko, V. P. Savchyn, J. M. Stakhira, *Mater. Chem. Phys.* **2000**, *65*, 130–135.
[26] O. A. Balitskii, R. V. Lutsiv, V. P. Savchyn, J. M. Stakhira, *Mater. Sci. Eng. B* **1998**, *56*, 5–10.
[27] P. H. Ho, Y. R. Chang, Y. C. Chu, M. K. Li, C. A. Tsai, W. H. Wang, C. H. Ho, C. W. Chen, P. W. Chiu, *ACS Nano* **2017**, *11*, 7362–7370.
[28] I. Miyake, T. Tanpo, C. Tatsuyama, *Jpn. J. Appl. Phys.* **1984**, *23*, 172.
[29] C. H. Ho, C. H. Lin, Y. P. Wang, Y. C. Chen, S. H. Chen, Y. S. Huang, *ACS Appl. Mater. Interfaces* **2013**, *5*, 2269–2277.
[30] L. Shi, Q. H. Zhou, Y. H. Zhao, Y. X. Ouyang, C. Y. Ling, Q. Li, J. L. Wang, *J. Phys. Chem. Lett.* **2017**, *8*, 4368–4373.
[31] R. Lewandowska, R. Bacewicz, J. Filipowicz, W. Paszkowicz, *Mater. Res. Bull.* **2001**, *36*, 2577–2583.
[32] G. Almeida, S. Dogan, G. Bertoni, C. Giannini, R. Gaspari, S. Perissinotto, R. Krahne, S. Ghosh, L. Manna, *J. Am. Chem. Soc.* **2017**, *139*, 3005–3011.
[33] A. Tuxen, J. Kibsgaard, H. Gøbel, E. Lægsgaard, H. Topsøe, J. V. Lauritsen, F. Besenbacher, *ACS Nano* **2010**, *4*, 4677–4682.
[34] Y. G. Li, H. L. Wang, L. M. Xie, Y. Y. Liang, G. S. Hong, H. J. Dai, *J. Am. Chem. Soc.* **2011**, *133*, 7296–7299.
[35] D. Merki, S. Fierro, H. Vrubel, X. L. Hu, *Chem. Sci.* **2011**, *2*, 1262–1267.
[36] G. Q. Li, D. Zhang, Q. Qiao, Y. F. Yu, D. Peterson, A. Zafar, R. Kumar, S. Curtarolo, F. Hunte, S. Shannon, Y. M. Zhu, W. T. Yang, L. Y. Cao, *J. Am. Chem. Soc.* **2016**, *138*, 16632–16638.
[37] J. Gao, B. C. Li, J. W. Tan, P. Chow, T. M. Lu, N. Koratkar, *ACS Nano* **2016**, *10*, 2628–2635.
[38] S. H. Chae, Y. J. Jin, T. S. Kim, D. S. Chung, H. Y. Na, H. G. Nam, H. Kim, D. J. Perello, H. Y. Jeong, T. H. Ly, Y. H. Lee, *ACS Nano* **2016**, *10*, 1309–1316.
[39] P. Budania, P. Baine, J. Montgomery, C. McGeough, T. Cafolla, M. Modreanu, D. McNeill, N. Mitchell, G. Hughes, P. Hurley, *MRS Commun.* **2017**, *7*, 813–818.
[40] A. Politano, G. Chiarello, R. Samnakay, G. Liu, B. Gürbulak, S. Duman, A. A. Balandin, D. W. Boukhvalov, *Nanoscale* **2016**, *8*, 8474–8479.
[41] Q. H. Zhou, Q. Chen, Y. L. Tong, J. L. Wang, *Angew. Chem. Int. Ed.* **2016**, *55*, 11437–11441; *Angew. Chem.* **2016**, *128*, 11609–11613.
[42] Z. H. Hu, Q. Li, B. Lei, Q. H. Zhou, D. Xiang, Z. Y. Lyu, F. Hu, J. Y. Wang, Y. J. Ren, R. Guo, E. Goki, L. Wang, C. Han, J. L. Wang, W. Chen, *Angew. Chem. Int. Ed.* **2017**, *56*, 9131–9135; *Angew. Chem.* **2017**, *129*, 9259–9263.

Manuscript received: January 9, 2023
Accepted manuscript online: March 2, 2023
Version of record online: March 20, 2023